ANNUAL REVIEWS

Annual Review of Nuclear and Particle Science

Study of the Strong Interaction Among Hadrons with Correlations at the LHC

L. Fabbietti, V. Mantovani Sarti, and O. Vázquez Doce

Physik-Department, Technische Universität München, 85748 Garching, Germany; email: laura.fabbietti@ph.tum.de

Annu. Rev. Nucl. Part. Sci. 2021. 71:377–402

The *Annual Review of Nuclear and Particle Science* is online at nucl.annualreviews.org

https://doi.org/10.1146/annurev-nucl-102419-034438

Keywords

strong interaction, correlations, hyperon, kaon, nuclear physics, femtoscopy, lattice QCD, bound state, chiral effective field theory, neutron stars

Abstract

The strong interaction among hadrons has been measured in the past by scattering experiments. Although this technique has been extremely successful in providing information about the nucleon–nucleon and pion–nucleon interactions, when unstable hadrons are considered the experiments become more challenging. In the last few years, the analysis of correlations in the momentum space for pairs of stable and unstable hadrons measured in *pp* and *p*+Pb collisions by the ALICE Collaboration at the LHC has provided a new method to investigate the strong interaction among hadrons. In this article, we review the numerous results recently achieved for hyperon–nucleon, hyperon–hyperon, and kaon–nucleon pairs, which show that this new method opens the possibility of measuring the residual strong interaction of any hadron pair.

Contents

1. INTRODUCTION

The study of the residual strong interaction among hadrons (colorless bound states of quarks and antiquarks) is still an open topic in nuclear physics. While the Standard Model of elementary particle physics provides a satisfactory description at the quark level in the high-energy regime, the low-energy processes that characterize the interaction among hadronic degrees of freedom are not yet described by a fundamental theory and are often difficult to access experimentally.

Hadron–hadron interactions have been studied in the past by means of scattering experiments at low energies (below the nucleon mass) for both stable and unstable beams. A reasonable quantity of scattering data (roughly 8,000 data points) (1, 2) is available for nucleon–nucleon (*NN*) reactions, but for kaons (mesons with one strange quark) and hyperons (baryons with at least one strange quark), the beam realization is more challenging. Kaon–nucleon interactions can be studied because the necessary secondary beams are accessible (3, 4), but for hyperon–nucleon reactions, the data are scarcer (17 data points) (5–7) because of the unstable nature of the hyperon beams, which is due to weak and electromagnetic decays. The lack of statistics in reactions that involve unstable hadrons affects the current description of the corresponding strong interaction from a theoretical point of view. If we consider only hadrons that contain *u*, *d*, and *s* quarks, most of the predicted interactions are not constrained experimentally. This not only represents a limit for nuclear physics but also has implications for astrophysics. Neutron stars (NSs), for example, could be constituted from nucleons, hyperons, and kaons, and their properties strictly depend on the interactions among these hadrons (8–10). Although the dense environment present within NSs is not easy to realize under controlled conditions with terrestrial experiments, the study of two- and three-body interactions among neutrons, protons, hyperons, and kaons in vacuum drives the equation of state (EoS) of NSs. In this review, we focus on the novel input provided by the ALICE experiment regarding the topic of interactions among nucleons, hyperons, and kaons by means of the femtoscopic method applied to data from ultrarelativistic *pp* and *p*+Pb collisions at the LHC.

Equation of state (EoS): thermodynamic relation among pressure, energy density, and temperature describing the properties of nuclear matter under extreme conditions (high T or high density); strongly dependent on the constituents and interactions among them

Historically, the femtoscopic technique can be traced back to the first measurements of particle interferometry with photons, which were performed by Hanbury Brown & Twiss (11) during the 1950s to determine the size of stars. The same idea has been subsequently applied to pairs of identical particles in elementary and heavy-ion collisions (HICs) (12–17) and has proved to be a useful tool to determine the space-time structure of the emitting source. The analysis of pion or kaon pairs, where the quantum statistics together with the Coulomb interaction characterize the shape of the correlations, has dominated femtoscopic studies in the last three decades. Results from intermediate-energy HICs at the Bevalac in the mid-1980s quantitatively showed that the spatial dynamics of the system could be probed by femtoscopy, and in the following years femtoscopic studies have been performed in several different experiments and energy ranges, including SIS ($\sqrt{s_{NN}} = 1$–3 GeV) (18, 19), AGS ($\sqrt{s_{NN}} = 5$–10 GeV) (20, 21), SPS ($\sqrt{s_{NN}} = 17$ GeV) (22, 23), and, more recently, RHIC ($\sqrt{s_{NN}} = 200$ GeV) (24) and the LHC ($\sqrt{s_{NN}} = 5$–13 TeV) (25).

The abundance of collected data made it possible to study the three-dimensional evolution of the particle-emitting source, which is helpful in characterizing the kinematic freeze-out of different hadron species. The typical source sizes measured in HICs range from 2 fm for SIS energies up to 5–6 fm for measurements at RHIC and the LHC (26, 27).

In the last two decades, much effort has been put into using femtoscopy to understand and study the strong interaction among hadrons (28). This line of research was pioneered in the last decade (18, 29) and then developed further by the STAR Collaboration in studies of $\Lambda\Lambda$ (30), $\bar{p}\bar{p}$ (31), and, more recently, $p\Omega^-$ (32) correlations measured in Au+Au collisions at $\sqrt{s_{NN}} = 200$ GeV. These studies showed the limits of the method applied to ultrarelativistic HICs, where the average interparticle distance of 7–8 fm reduces the sensitivity to the short-range strong interaction. This distance of particles at kinetic freeze-out is obtained from the probability density distribution for Gaussian sources with radii of 3–4 fm (33). This research also demonstrated that interaction studies require extremely high purity for particle identification and detailed treatment of the residual background (34). Following the same approach, the ALICE Collaboration successfully extracted for the first time the ΛK and baryon–antibaryon scattering parameters from Pb+Pb collisions at $\sqrt{s_{NN}} = 2.76$ and 5.02 TeV (35, 36). The results from the ALICE and STAR Collaborations provided a first proof that the correlation function can be exploited to infer information on the underlying strong interaction.

In the last 3 years, the ALICE Collaboration has applied the femtoscopic technique to *pp* and *p*+Pb collisions and shown for the first time the potential to precisely assess the strong interaction among stable and unstable hadrons. The average interparticle distance obtained from such collisions at the LHC is about 1 fm and is therefore comparable to the range of the strong potentials. This feature, combined with the excellent particle identification provided by the ALICE apparatus and the extensive statistics collected during the LHC Run 2 data taking, has allowed precise measurement of the following interactions: pp (37), K^+p and K^-p (38), $p\Lambda$ (37), $p\Sigma^0$ (39), $\Lambda\Lambda$ (40), $p\Xi^-$ (41), and $p\Omega^-$ (42). This review describes the main features of the femtoscopic technique, the advantages of using it in small colliding systems, and the results obtained in the study of hadron–hadron interactions with strangeness.

The review is structured as follows. The femtoscopic method is presented in Section 2. In Section 3, the modeling of the emitting source in *pp* collisions is presented, and the main features of femtoscopy in elementary collisions are discussed. The main results on hadron–hadron interactions obtained with the ALICE femtoscopic measurements are discussed in Section 4 with a particular emphasis on hyperon–nucleon systems (Section 4.1), the possible detection of bound states (Section 4.2), and coupled-channel dynamics (Section 4.3). In Section 5, the possible implications for the presence of hyperons inside NSs are considered. Section 6 discusses the future prospects for femtoscopic achievements in the next ALICE data-taking periods (Runs 3

and 4), and Section 7 summarizes the current state of the field and points to future theoretical and experimental developments.

2. METHODOLOGY

The fundamental quantity to be measured in femtoscopy is the correlation function. It is expressed as a function of the relative distance between two particles $\mathbf{r}^*$ and their reduced relative momentum, $k^* = |\mathbf{p}_2^* - \mathbf{p}_1^*|/2$ in the pair rest frame, with $\mathbf{p}_1^* = -\mathbf{p}_2^*$, by the Koonin–Pratt formula (33, 43):[1]

$$C(k^*) = \int S(\mathbf{r}^*)|\psi(\mathbf{r}^*, \mathbf{k}^*)|^2 \mathrm{d}^3 r. \quad 1.$$

The first term in Equation 1, $S(\mathbf{r}^*)$, describes the source that emits the particles; the second term contains the interaction part via the two-particle wave function $\psi(\mathbf{r}^*, \mathbf{k}^*)$. The shape of the correlation function is determined by the characteristics of the source function and the sign and strength of the interaction.

An analytical model by Lednický & Lyuboshitz (44) exists to compute this correlation function. The Lednický–Lyuboshitz (LL) model assumes a Gaussian profile that depends only on the magnitude of the relative distance for the source function

$$S(r^*) = \left(4\pi r_0^2\right)^{-3/2} \cdot \exp\left(-\frac{r^{*2}}{4r_0^2}\right), \quad 2.$$

where r_0 is the radius parameter that defines the size of the source. The effective range approximation is used to define the complex scattering amplitude as

$$f(k^*)^S = \left(\frac{1}{f_0^S} + \frac{1}{2} d_0^S k^{*2} - ik^*\right)^{-1}, \quad 3.$$

where S is the total spin of the particle pair, and f_0^S and d_0^S are the scattering length and the effective range, respectively. The correlation function for uncharged particles then becomes

$$C(k^*)_{\mathrm{LL}} = 1 + \sum_S \rho_S \left[\frac{1}{2}\left|\frac{f(k^*)^S}{r_0}\right|^2 \left(1 - \frac{d_0^S}{2\sqrt{\pi} r_0}\right) + \frac{2\Re f(k^*)^S}{\sqrt{\pi} r_0} F_1(2k^* r_0) - \frac{\Im f(k^*)^S}{r_0} F_2(2k^* r_0)\right],$$

where $F_1(2k^*r_0)$ and $F_2(2k^*r_0)$ are analytical functions that result from the Gaussian source approximation, and ρ_S is the pair fraction that is emitted into the spin state S.

Since the LL approach is based on the effective range expansion, it presents limitations for small systems because it does not account for the details of the wave function at small distances, where the effect of the strong potential is more pronounced. Such limitations motivated the development of the Correlation Analysis Tool using the Schrödinger equation (CATS) framework (45), which provides a numerical recipe for the calculation of the exact solution of the two-body nonrelativistic Schrödinger equation given a local interaction potential. The resulting relative wave function combined with a parameterization of the source makes it possible to compute predictions for the different correlation functions by means of Equation 1. The CATS framework can account

[1]The relative momentum formula in terms of the invariant relative momentum q_{inv} reads $k^* = \sqrt{\frac{a^2 - m_1^2 m_2^2}{2a + m_1^2 + m_2^2}}$, $a = \frac{1}{2}(q_{\mathrm{inv}}^2 + m_1^2 + m_2^2)$ and $q_{\mathrm{inv}}^2 = |\mathbf{p}_1 - \mathbf{p}_2|^2 - |E_1 - E_2|^2$, where m_1 and m_2 are the masses of the particles in the pair and $\mathbf{p}_1$ and $\mathbf{p}_2$ are the particle momenta in the laboratory reference system. If the two particles have the same mass, then $k^* = \frac{q_{\mathrm{inv}}}{2}$.

for both short-range potentials and the Coulomb long-range interaction as well as different parameterizations of the source function beyond the Gaussian approximation. The LL model is also implemented in CATS with the scattering length f_0^S and the effective range d_0^S used as input for the description of the interaction.

The features of the interaction are mapped into the corresponding correlation function. In particular, the effects of the final-state interactions are more evident in the correlation function at small k^* values. A repulsive interaction, with positive values of the local potentials, implies a correlation function with values between 0 and 1. For an attractive interaction, in contrast, the resulting correlation function yields values above unity. This intuitive picture is modified, however, if the attraction is strong enough to accommodate the presence of a bound state. In this case, a depletion in the values of the correlation function can be seen, depending on the binding energy (BE) (46). This depletion occurs because the pairs that form the bound state are lost to the correlation as they result in a different final state.

The strength of the correlation can also be enhanced by small sizes of the source function, as discussed below. Other effects, which are not caused by the final-state interaction, can be visible at different k^* ranges of the correlation function, such as quantum mechanical interference, resonances, and conservation laws.

Figure 1 demonstrates the sensitivity of the femtoscopic method applied to small colliding systems for the study of the strong interaction assuming an attractive, repulsive, or binding potential. The left lower panel of **Figure 1*a*** shows the corresponding squared modulus of the wave function together with the density distribution according to Gaussian profiles with two different

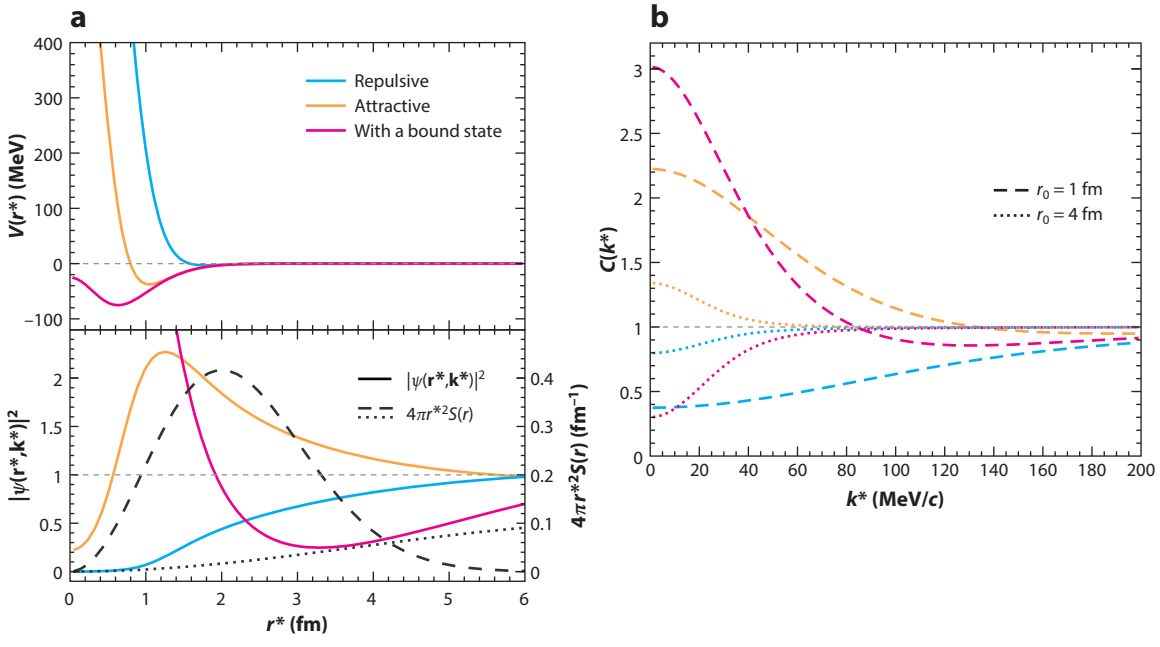

Figure 1

(*a*, *top*) Examples of an attractive potential (*orange*), a repulsive potential (*blue*), and a potential with a shallow bound state (*pink*). (*a*, *bottom*) Modulus squared of the total wave functions $|\psi(\mathbf{r}^*, \mathbf{k}^*)|^2$, as a function of the relative distance r, obtained by solving the Schrödinger equation employing the CATS framework for the three example potentials. In the same plot, the profile of the emitting source is shown for 1 fm (*dashed black line*) and 4 fm (*dotted black line*). (*b*) Resulting correlation function $C(k^*)$ for each interaction, evaluated for the two different source sizes, $r_0 = 1$ fm (*dashed lines*) and 4 fm (*dotted lines*).

radii ($r_0 = 1$ and 4 fm). The sensitivity of the method to study the strong interaction depends on the overlap of the square of the wave function with the source density distribution. Typical sizes of the parameter $r_0 = 3$–6 fm describe the source formed in Pb+Pb collisions at the LHC (47), while *pp* and *p*+Pb collisions at the same energies lead to the formation of sources with much smaller radii (between 1 and 1.5 fm) (37, 41). One can see that for HICs, the overlap is minimal, and hence the sensitivity to the short-range interaction is very limited. The typical features of the attractive and repulsive interactions and the presence of the bound state are much more pronounced in the case of the small source size. The less pronounced correlation function obtained with the larger source is difficult to measure with sufficient precision.

Primary and secondary particles: the fraction f_i of primary and secondary (i.e., produced in a decay) particles entering the λ_{ij} parameters is evaluated from experimental data considering weak and electromagnetic decays and fake candidates for each hadron species

In the case of the bound state, the reason why the correlation function flips around one for different source sizes is that the wave function is very sharply peaked toward distances equal to zero because of the much stronger localization of the bound state. This translates to an increased correlation for small radii, whereas for large radii only the asymptotic part of the wave function, which is depleted because of conservation of probability, affects the correlation function and brings it below one.

The method used by the ALICE Collaboration to study interactions among hadrons is to compare the theoretical expectation for the correlation function with a correlation function obtained experimentally. The experimental correlation function is obtained as the ratio of the relative momentum distribution of pairs of particles produced in the same event (SE), which constitutes the sample of correlated pairs, to a reference distribution obtained by combining particles produced in different collisions, using the so-called mixed event (ME) technique:

$$C(k^*) = \xi(k^*) \cdot \frac{N_{\mathrm{SE}}(k^*)}{N_{\mathrm{ME}}(k^*)}. \qquad 4.$$

The corrections for experimental effects are denoted by $\xi(k^*)$ in Equation 4. Such corrections take into account the finite experimental resolution and corrections to the ME distributions to ensure the same experimental conditions and normalization as for the SEs. In general, they do not account for the contributions from misidentification, weak decays, or residual background induced by mini-jets and event-by-event momentum conservation. These effects are accounted for in the fit of the correlation functions.

The experimental correlation function is further distorted by two distinct mechanisms. The sample of particle pairs can include primary particles as well as misidentified particles and secondary particles from weak decays of resonances. This introduces contributions of different, nongenuine pairs into the measured correlation function. The treatment of these contributions is described in detail in Reference 37, so here we only briefly sketch the procedure. The contributions of the different nongenuine and genuine correlations to the total experimental correlation are indicated by weights called λ parameters. These λ parameters are obtained by pairing single-particle properties, such as the purity (P) and feed-down fractions (f): $\lambda_{ij} = P_i P_j f_i f_j$. The total correlation function can then be decomposed as

$$C(k^*) = 1 + \lambda_{\mathrm{genuine}} \cdot [C_{\mathrm{genuine}}(k^*) - 1] + \sum_{ij} \lambda_{ij} [C_{ij}(k^*) - 1], \qquad 5.$$

where i and j denote all possible impurity and feed-down contributions.

The correlation functions measured in the ALICE experiment are compared with theoretical expectations obtained according to Equation 5. For this task, the λ parameters are obtained from experimental data when possible (e.g., purity, fractions of secondary particles). In addition, the experimental effects denoted by $\xi(k^*)$ in Equation 4 are taken into account when modeling the theoretical correlation function. The only exception is the study of the $p\Xi$ and $p\Omega^-$ correlation functions in *pp* collisions at 13 TeV published in Reference 42, in which the experimental data

have been unfolded for all effects and directly compared with the genuine theoretical correlation function.

To account for residual contributions from the mini-jet background to the final correlations, a baseline with free parameters is multiplied with the correlation function $C(k^*)$ used to fit the experimental data (37). This baseline assumes different shapes depending on the pair of interest, but it contributes at most a few percent to the global correlation strength (39, 41).

Transverse mass: the transverse mass of the pair is defined as $m_T = \sqrt{{k_T}^2 + m^2}$, where m is the average mass of the particle pair and $k_T = \frac{|\mathbf{p}_{T,1} + \mathbf{p}_{T,2}|}{2}$ is the relative transverse momentum

3. DETERMINATION OF THE PARTICLE-EMITTING SOURCE

After the collision and the completion of the hadronization processes, particles might undergo some inelastic collisions, but shortly after their production they propagate freely toward the detectors. The distribution of the space coordinates at which the different particles assume their primary momentum values characterizes the particle-emitting source. Understanding this source for the selected colliding system is mandatory in order to extract information on the underlying strong interaction.

Gaussian source profiles in one and three dimensions are typically assumed in femtoscopic studies performed in HICs (33, 48). However, the presence of a collective expansion can introduce correlations between the position and momentum of the emitted particles. This effect can be seen as a decrease of the extracted Gaussian radii with increasing pair transverse momentum k_T (33, 49). Experimentally, a common scaling of the source size with the transverse mass of proton and kaon pairs has been seen in Pb+Pb collisions (50).

High-multiplicity *pp* collisions and heavy-ion systems exhibit similar behavior in several related measured quantities, such as angular correlations and strangeness production (51–54). Hence, a similar transverse mass (m_T) scaling of the source size as observed in large systems is expected to apply in *pp* collisions. Measurements of this kind in small systems are currently available for light meson pairs ($\pi\pi$, KK) (55–59), accessing only low values of m_T but indicating a dependence of the radius on the transverse mass.

Recently, similar studies of baryon–baryon femtoscopy, for *pp* and $p\Lambda$ pairs, were conducted in high-multiplicity *pp* collisions, and these studies provided for the first time a quantitative measurement of a common scaling in the range $m_T = 1.3$–2.4 GeV/c^2 (60). The explicit inclusion of strongly decaying resonances proved to be a fundamental ingredient for the description of the data. The presence of feed-down from strong resonances had already been suggested as a possible explanation for the description of the different scaling of radii extracted in $\pi\pi$ correlations seen in HICs (61, 62). A similar broken scaling is observed in *pp* collisions for $p\Lambda$ pairs when a Gaussian source profile is assumed and feed-down effects are not taken into account (60). The extracted $p\Lambda$ radii are typically 20% larger with respect to the *pp* pair results. In the spirit of testing the hypothesis of a common source for small colliding systems, a complete modeling of the resonance contributions has to be performed.

The emitting source $S(r^*)$ used to fit *pp* and $p\Lambda$ correlation functions with Equation 1 is composed of a Gaussian core of width r_{core} (see Equation 2), related to the emission of all primordial particles,

$$S_{\text{prim}}\left(\mathbf{r}^*_{\text{core}}\right) = \left(4\pi r^2_{\text{core}}\right)^{-3/2} \cdot \exp\left(-\frac{{\mathbf{r}^*_{\text{core}}}^2}{4r^2_{\text{core}}}\right), \qquad 6.$$

and of an exponential distribution originating from strong decays of resonances with a specific lifetime τ_{res}.

The modification of the relative distance $\mathbf{r}^*$ of the particle in the pair, entering the final description of the source, linearly depends on the core distance $\mathbf{r}^*_{\text{core}}$ and also on the distances $\mathbf{r}^*_{\text{res},i}$

traveled by the resonances $i = 1, 2$ of momentum $\mathbf{p}^*_{\mathrm{res},i}$, mass $M_{\mathrm{res},i}$, and flight time $t_{\mathrm{res},i}$ sampled from the exponential distribution based on the corresponding lifetime $\tau_{\mathrm{res},i}$:

$$\mathbf{r}^* = \mathbf{r}^*_{\mathrm{core}} + \sum_i \mathbf{r}^*_{\mathrm{res},i}, \quad \mathbf{r}^*_{\mathrm{res},i} = \frac{\mathbf{p}^*_{\mathrm{res},i}}{M_{\mathrm{res},i}} t_{\mathrm{res},i}. \tag{7.}$$

These latter quantities, which are related to the resonances feeding to p and Λ, depend on the resonance yields and kinematics. The absolute value $r^* = |\mathbf{r}^*|$ needs to be evaluated for the one-dimensional source function $S(r^*)$. From the definitions in Equation 7, the necessary ingredients are r^*_{core}; the momenta, masses, and lifetimes of the resonances; the angles formed by $\mathbf{r}^*_{\mathrm{core}}$; and the resonance distances $\mathbf{s}^*_{\mathrm{res},1}$ and $\mathbf{s}^*_{\mathrm{res},2}$.

The amount and type of resonances can be estimated from calculations based on the statistical hadronization model (63–65) and are found to be similar (∼65%) between the two particles, coming mostly from Δ for protons and from Σ^* for Λ. This different composition of secondary particles translates into a significantly larger average lifetime and average mass ($M_{\mathrm{res}} = 1.46$ GeV/c^2, $c\tau_{\mathrm{res}} = 4.7$ fm) for Λ hyperons with respect to protons ($M_{\mathrm{res}} = 1.36$ GeV/c^2, $c\tau_{\mathrm{res}} = 1.6$ fm), explaining qualitatively the larger effective source obtained in Reference 60. The remaining kinematics parameters—namely, the momenta of the resonances and their relative orientation with respect to $\mathbf{r}^*_{\mathrm{core}}$—are determined from transport model simulations within the EPOS framework (66).

The total source can be finally decomposed, depending on the origin of each particle in the pair (either primary or from a resonance), as follows:

$$\begin{aligned} S(r^*) \; &= P_{\mathrm{prim}} P_{\mathrm{prim}} \times S_{\mathrm{prim\text{-}prim}}(r^*) + P_{\mathrm{prim}} P_{\mathrm{res}} \times S_{\mathrm{prim\text{-}res}}(r^*) \\ &+ \; P_{\mathrm{res}} P_{\mathrm{prim}} \times S_{\mathrm{res\text{-}prim}}(r^*) + P_{\mathrm{res}} P_{\mathrm{res}} \times S_{\mathrm{res\text{-}res}}(r^*). \end{aligned} \tag{8.}$$

Here, P_{prim} and P_{res} are the fractions of primordial and resonance contributions estimated from thermal model calculations. Once all the resonance dynamics and composition for the considered pair are accounted for, the Gaussian source size r_{core}, which is related to the prompt emission of particles, remains as the only free parameter to be determined via a fit to the data.

A differential m_{T} analysis has been performed on pp and $p\Lambda$ correlations, and the core radius has been extracted in each m_{T} bin. **Figure 2*a*** shows the resulting m_{T}-integrated pp correlation function obtained assuming the core resonance source model. The genuine pp term of the correlation is modeled using the CATS framework, assuming the Argonne v_{18} (67) as the strong potential (including S-, P-, and D-waves) and including the Coulomb interaction along with the proper quantum statistical antisymmetrization of the wave function. The underlying strong interaction between protons is known with high precision and is accurately described by the Argonne v_{18} potential (67), allowing for a reliable determination of the r_{core} parameter. The data are nicely reproduced by the modeled correlation, and the same fitting procedure has been adopted in the single m_{T} bins, leading to similar results. The $p\Lambda$ interaction is less constrained (5–7, 37, 68), and hence both leading order (LO) (69) and next-to-leading order (NLO) (70) chiral effective field theory (χEFT) calculations have been employed.

Figure 2*b* shows the m_{T} dependence of the extracted core radii for the two pairs. As can be clearly seen, the inclusion of resonances in the modeling of the source provides a common m_{T} scaling for both baryon–baryon pairs, providing the first quantitative evidence of a common emitting source in small systems. This result delivers a fundamental input to be used in the investigation of the strong interaction by means of femtoscopy because it allows one to fix the source for any baryon–baryon pair, given the $\langle m_{\mathrm{T}} \rangle$ of the pair and the resonance contributions.

If the source $S(r^*)$ is under control from the analysis of particle species for which the final-state interaction is known, then the relative wave function $\psi(\mathbf{r}^*, \mathbf{k}^*)$ and hence the interaction for other

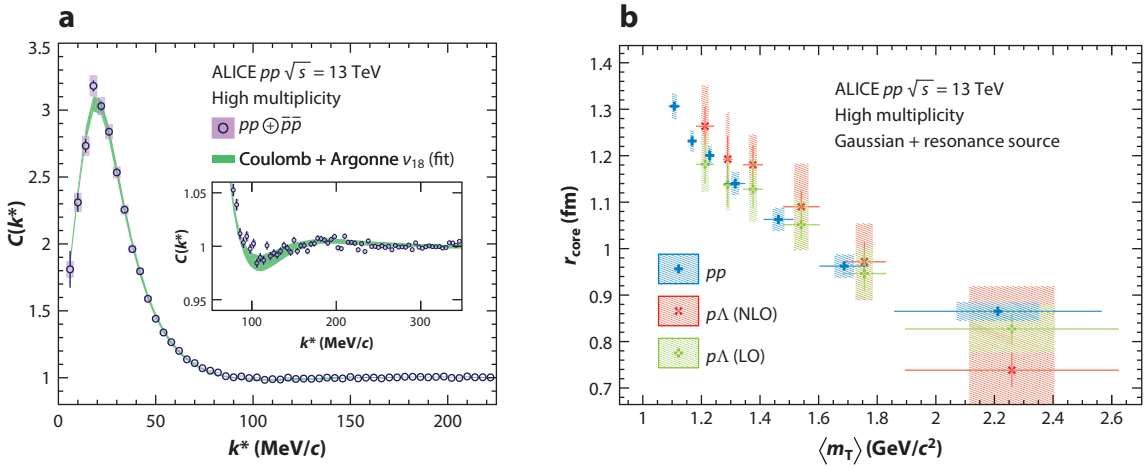

Figure 2

(*a*) Transverse mass (m_T)-integrated *pp* correlation as a function of k^* measured in high-multiplicity *pp* collisions, including the contributions from strong resonances. The width of the green band represents one standard deviation of the systematic uncertainty of the fit. (*b*) Gaussian core radius (r_{core}) as a function of $\langle m_T \rangle$. Blue crosses correspond to the *pp* correlation function fitted with the Argonne v_{18} potential (67) as the strong potential. The green squared crosses and red diagonal crosses result from fitting the $p\Lambda$ correlation functions with the strong chiral effective field theory at LO (69) and NLO (70), respectively. In both panels, statistical uncertainties (*error bars*) and systematic uncertainties (*shaded boxes*) are shown separately. Abbreviations: LO, leading order; NLO, next-to-leading order. Panel *a* adapted from Reference 39 (CC BY 4.0). Panel *b* adapted from Reference 60 (CC BY 4.0).

species can be determined by studying the correlation function (see Equation 1). Furthermore, the small values found for the core radius r_{core} imply that *pp* collisions at the LHC are excellent systems through which to study to short-range strong interaction.

4. PROBING THE STRONG INTERACTION FOR STRANGE HADRONS

The interaction between strange hadrons and nucleons is not well constrained by experimental data. In particular, the unstable nature of hyperons complicates the investigation of two- and three-body interactions. The high statistics collected for all hyperon species in *pp* and *p*+Pb collisions measured by the ALICE Collaboration during Runs 1 and 2 at the LHC allowed unprecedented precision in the study of different interactions, including combinations that already had been studied in the past by means of scattering experiments ($pK^{\pm}$ and $p\Lambda$) (5–7, 68, 71–74) or that never had been measured before ($p\Xi^-$ and $p\Omega^-$).

The identification, tracking, and momentum resolution provided by the ALICE experiment for all charged particles make it possible to study correlation functions down to relative momenta of 4–10 MeV/*c*. A precise measurement of the correlation function in this momentum range is necessary to study the details of the strong interaction. Moreover, the large quantity of hyperons, including species such as Ξ and Ω, makes it possible to measure hadron pairs not accessible in the standard scattering experiments. The measurement of these hyperons also allows one to test predictions from lattice QCD for interactions with nucleons since, for such heavy hyperons, the calculation results are rather solid (75).

The femtoscopic measurements performed in small colliding systems such as *pp* and *p*+Pb grant access to the short-range strong interaction, as described above in Section 2. In the sections below, we discuss in detail different features, such as coupled-channel effects and formation of bound states, that arise from the short-range dynamics of hadron–hadron potentials.

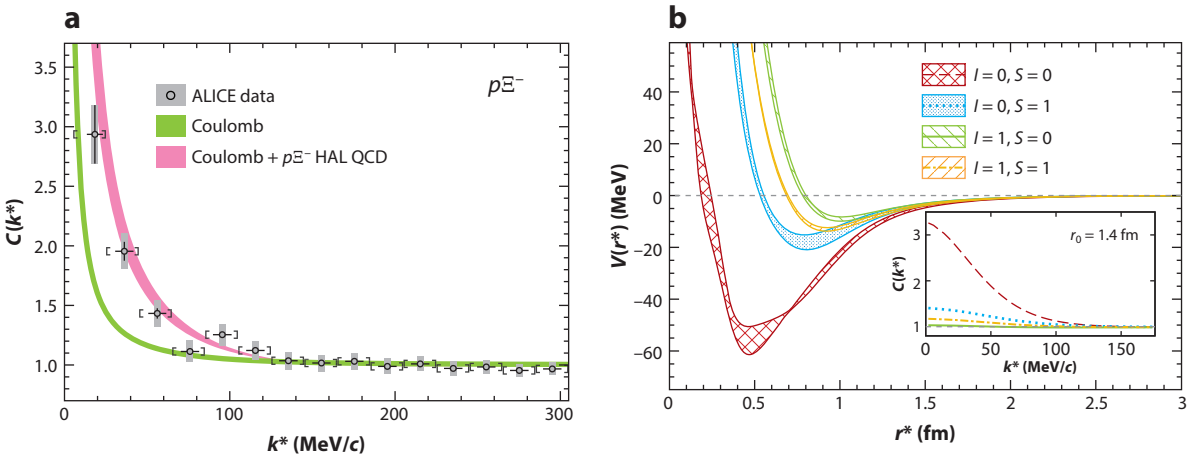

Figure 3

(*a*) The $p\Xi^-$ correlation function measured in *pp* collisions at $\sqrt{s} = 13$ TeV (42) recorded with a high-multiplicity trigger. The experimental data are shown by open circles; error bars indicate statistical errors, and gray boxes indicate systematic errors. The green curve represents the predicted correlation function assuming only the Coulomb interaction. The pink curve shows the prediction obtained considering the Coulomb and strong interaction provided by the HAL QCD Collaboration (75). (*b*) Strong potentials for the different spin and isospin configurations of the $p\Xi^-$ interaction as a function of the interparticle distance (41). The inset shows the corresponding correlation functions, which have been evaluated using a Gaussian source with a radius of $r_0 = 1.4$ fm. Panel *a* adapted from Reference 42 (CC BY 4.0). Panel *b* adapted from Reference 41 (CC BY 4.0).

4.1. Study of the Hyperon–Nucleon Interaction

One of the challenging measurements achieved by applying the femtoscopic technique to *pp* and *p*+Pb collisions and interpreting the observables with the help of the CATS framework is the study of the $p\Xi^-$ interaction. The $\Xi^\pm$ hyperons are reconstructed by exploiting the weak decays $\Xi^\pm \rightarrow \Lambda + \pi^\pm$ and $\Lambda \rightarrow p + \pi^-$. A total invariant mass resolution below 2 MeV/c^2 (76) is obtained for the reconstructed $\Xi^\pm$, and the obtained $p\Xi^- \oplus \bar{p}\Xi^+$ correlation function is shown in **Figure 3*a*** (the data have been corrected for experimental effects). **Figure 3*b*** shows the strong potentials predicted by the HAL QCD Collaboration for the four allowed spin and isospin states of the $p\Xi^-$ system. One can see that for all cases, an attractive interaction and a repulsive core characterize the potentials.

All the potentials shown in **Figure 3*b*** are similar at interparticle distances above 1.5 fm, but the corresponding correlation functions are very different. This difference is due to the sensitivity of the method to the small distances (below 1 fm) that are typical for *pp* and *p*+Pb collisions. The total $p\Xi^-$ correlation function shown in **Figure 3*a*** is obtained by including the strong and the Coulomb potentials in the Schrödinger equation and combining the correlation functions for each of the allowed spin and isospin states weighted by the proper Clebsch–Gordan coefficients, following $C_{p\Xi^-} = \frac{1}{8}C_{(I=0,S=0)} + \frac{3}{8}C_{(I=0,S=1)} + \frac{1}{8}C_{(I=1,S=0)} + \frac{3}{8}C_{(I=1,S=1)}$. The source size for the $p\Xi^-$ pair has been evaluated following the model described in Section 3, considering the average m_T of the pair and the strong resonance contribution for the protons, leading to a value of $r_0 = 1.02 \pm 0.05$ fm. The total $p\Xi^-$ correlation for the Coulomb and HAL QCD strong interaction shown in **Figure 3*a*** lies above the Coulomb predictions, demonstrating the presence of an additional attractive strong interaction. These data provide a reference that can now be employed to test any theoretical calculation of the $p\Xi^-$ interaction.

The $p\Xi^-$ system presents two inelastic channels, $n\Xi^0$ and $\Lambda\Lambda$, just below threshold and three others, $\Lambda\Sigma^0$, $\Sigma^0\Sigma^0$, and $\Sigma^+\Sigma^-$, well above threshold (77). The latter, since their opening occurs far away from the $p\Xi^-$ mass threshold and theoretical predictions indicate a shallow interaction for these pairs, will have a negligible effect on the $p\Xi^-$ correlation function. In the specific case of the $\Lambda\Lambda$ channel, precise femtoscopic measurements confirmed the weak strength of the strong interaction for these hyperons by means of hypernuclei data (78). Predictions based on chiral calculations for the $n\Xi^0$ channel show a visible effect in the $p\Xi^-$ correlation signal (77), but this coupling is not yet present in lattice QCD calculations. In the calculation that includes the strong interaction provided by the HAL QCD Collaboration (75) (see pink curve in **Figure 3*a***), the nondiagonal terms of the interactions that contain the contribution of coupled channels (see Section 4.3) are neglected. Nevertheless, a direct measurement of these inelastic contributions is necessary to draw solid conclusions.

4.2. Search for Bound States

The $\Lambda\Lambda$ interaction attracted the attention of both theoreticians and experimentalists many years ago (79) because of the possible existence of the H dibaryon: a bound state composed of six quarks (*uuddss*). From an experimental point of view, the $\Lambda\Lambda$ interaction was first addressed by studying the production of double-Λ hypernuclei. The measurement of the BE of the hypernucleus ${}^{\;\;6}_{\Lambda\Lambda}\mathrm{He}$ allowed the estimation of the $\Lambda\Lambda$ BE $= 6.91 \pm 0.6$ MeV (78). This value was considered as an upper limit for the H dibaryon. Direct searches for the decays $H \rightarrow \Lambda p\pi$ also were carried out (80), but they never delivered any evidence. A more recent upper limit evaluation of the bound state BE was obtained from a correlation analysis (40).

An analysis of HIC data to study such an interaction was also proposed (81), and the first attempt to investigate the $\Lambda\Lambda$ final state via correlations was carried out by the STAR Collaboration in Au+Au collisions at $\sqrt{s_{NN}} = 200$ GeV (82). This analysis delivered a scattering length of $f_0^{-1} = -0.91 \pm 0.31^{+0.07}_{-0.56}$ fm^{-1} and an effective range of $d_0 = 8.52 \pm 2.56^{+2.09}_{-0.74}$ fm. These values correspond to a repulsive interaction. However, it was shown that the values and sign of the scattering parameters strongly depend on the treatment of feed-down contributions from weak decays to the measured correlation. A reanalysis of the data outside the STAR Collaboration extracted a positive value for f_0^{-1} corresponding to a shallow attractive interaction potential (34). The $\Lambda\Lambda$ correlations measured by the ALICE Collaboration (37, 40) in pp collisions at $\sqrt{s_{NN}} = 7$ and 13 TeV and p+Pb collisions at $\sqrt{s_{NN}} = 5.02$ TeV were also employed to study the interaction, and the residual correlations were treated by means of a novel data-driven method. Since the statistics of the $\Lambda\Lambda$ pairs with small relative momentum were limited, instead of extracting the scattering parameters from the fit of the correlation function, a different approach was carried out (40). A scan of different combinations of scattering parameters (f_0^{-1}, d_0) in the range $f_0^{-1} \in [-2, 5]$ fm^{-1} and $d_0 \in [0, 18]$ fm was performed. For each combination of values of the scattering parameters, the correlation function was evaluated by using the LL method. The agreement with the experimental correlation function, using all data samples from pp collisions at $\sqrt{s} = 7$ and 13 TeV and p+Pb collisions at $\sqrt{s_{NN}} = 5.02$ TeV, was quantified in terms of a confidence level according to the method described in chapter 15.6.1 of Reference 83. The CATS framework was used to cross-check the results from the LL method; the differences in the correlation functions obtained using the two methods are negligible. The Gaussian source approximation employed in the LL method was also validated by cross-checks using the source profile predicted by the EPOS transport model (45, 66) and considering the effects of short-lived resonances. The results, expressed in number of standard deviations ($n\sigma$), are shown in **Figure 4*a***. The black hatched area in **Figure 4*a*** represents an unphysical region where the resulting correlation function becomes negative.

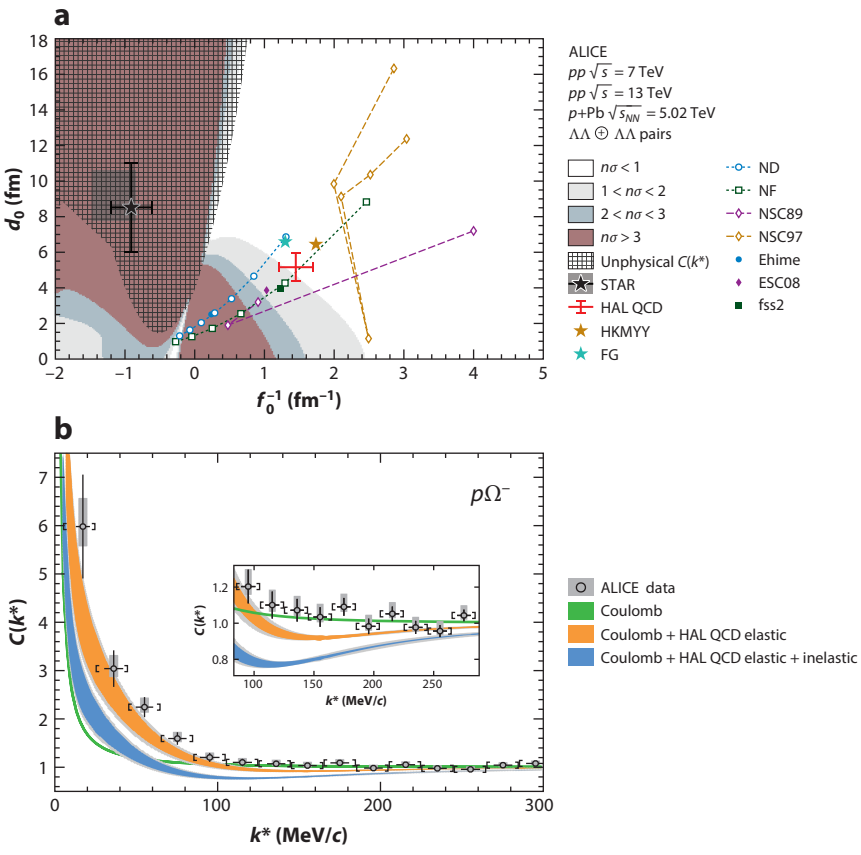

Figure 4

(*a*) Exclusion plot of the scattering parameters for the ΛΛ interaction evaluated by testing the different values against the ΛΛ correlation. The black hatched area represents the values for which the Lednický–Lyuboshitz model breaks down for the small source sizes considered and delivers unphysical correlation functions. (*b*) Correlation function of $p\Omega^-$ pairs measured in the ALICE experiment in high-multiplicity pp collisions at $\sqrt{s} = 13$ TeV (42). The experimental data are shown by open circles; error bars indicate statistical errors, and gray boxes indicate systematic errors. The green line represents the correlation function expected when taking into account only the Coulomb interaction; its width is determined by the uncertainty in the source radius. The blue and orange bands represent predictions considering both Coulomb and strong interactions by the HAL QCD Collaboration (92). The prediction represented by the orange band considers only the elastic contributions for the strong interaction. The prediction represented by the blue band considers elastic and inelastic contributions; the width of the blue band represents the uncertainties associated with the lattice QCD calculations, and the gray band represents, in addition, the uncertainties associated with the determination of the source radius. The source radius, determined experimentally, is 0.95 ± 0.06 fm. The inset shows in detail the correlation function around unity. Panel *a* adapted from Reference 40 (CC BY 4.0). Panel *b* adapted from Reference 42 (CC BY 4.0).

This analysis has made it possible to extend the constraint to the scattering parameters and the BE of the ΛΛ system. The data are compared with models predicting either a strong attractive interaction (84), a ΛΛ bound state (85, 86), or a shallow attractive interaction potential (87–90). Through the comparison shown in **Figure 4**, one can see that the data favor a shallow attractive interaction and are compatible in particular with the models that are in agreement with hypernuclei data (88, 89) and with the model that consists of preliminary lattice QCD calculations by the HAL

QCD Collaboration (90). The data exclude the region corresponding to a strongly attractive or a very weakly binding short-range (small $|f_0^{-1}|$ and small d_0) interaction, and the first results from the STAR Collaboration (82) corresponding to a repulsive interaction are also excluded. The data do not exclude a $\Lambda\Lambda$ bound state with a shallow binding (corresponding to negative f_0^{-1} and small d_0 values). The upper limit of the BE for the H dibaryon candidate can be evaluated by applying the effective range approximation and relating the parameters f_0^{-1} and d_0 to a corresponding BE via

$$\mathrm{BE}_{\Lambda\Lambda} = \frac{1}{m_\Lambda d_0^2}\left(1 - \sqrt{1 + 2d_0 f_0^{-1}}\right)^2. \qquad 9.$$

Several caveats apply to this expression (40) since the implied effective range expansion might not be suited to describing the bound state properties. An analysis of the 1σ region compatible with the existence of a bound state of the results shown in **Figure 4*a*** allows a BE, considering statistical and systematic uncertainties, of $\mathrm{BE} = 3.2^{+1.6}_{-2.4}(\mathrm{stat.})^{+1.8}_{-1.0}(\mathrm{syst.})$ MeV (40).

An additional final state suited to the search for a baryon–baryon bound state is the $p\Omega^-$ channel. Recent studies from phenomenological approaches (91) and first principles calculations (92) predict an attractive interaction potential at all distances between protons and Ω^- baryons. Both approaches also predict the existence of a $p\Omega^-$ bound state with BEs of the order of a few MeV. For the strong-only and strong + Coulomb BEs, the two models predict 0.1 and 1 MeV (91) and 1.54 and 2.46 MeV (92), respectively.

As pointed out in Section 2, the presence of a bound state manifests itself in a depletion of the correlation function with a strength that depends on the BE and the shape of the attractive potential. In the presence of shallow bound states, the correlation looks similar to that seen in the case of a strongly attractive interaction, but for more deeply bound states the correlation can also drop below unity.

The $p\Omega^-$ correlation function has been studied recently by the ALICE Collaboration (42) using data from high-multiplicity pp collisions at 13 TeV, and the results are shown in **Figure 4*b***. The data in the figure are corrected for feed-down contributions and experimental effects, such as resolution effects at very small k^* values, meaning that these data can be directly compared with any theoretical prediction given a known emitting source.

The data in **Figure 4*b*** are compared with the predicted correlation function from calculations on the lattice by the HAL QCD Collaboration (92) for a Gaussian source with a radius $r_0 = 0.95 \pm 0.06$ fm. The source characteristics have been determined according to the method explained in Section 3, for an $\langle m_\mathrm{T}\rangle$ of the $p\Omega^-$ pairs of 2.2 GeV/c, and taking into account the effect produced by short-lived resonances. In **Figure 4*b***, the difference between the blue and orange colored bands corresponding to the HAL QCD prediction reflects the current uncertainty of the calculations due to the presence of strangeness-rearrangement processes in the $p\Omega^-$ channel.

For the $p\Omega^-$ S-wave interaction, the total angular momentum J can take on values of $J = 2$ or $J = 1$. Processes such as $p\Omega^- \rightarrow \Xi\Lambda, \Xi\Sigma$ can occur (46), affecting the $p\Omega^-$ interaction in particular in the $J = 1$ channel. For the $J = 2$ channel, the presence of strangeness-rearrangement processes should be strongly suppressed since they are possible only through D-wave interaction processes. This $J = 2$ channel is, so far, the only channel calculated by the HAL QCD Collaboration (92). To compare the lattice QCD calculations with the ALICE data, two extreme assumptions are made for the description of the interaction in the $J = 1$ channel, following the method explained in Reference 46: (*a*) no strangeness-rearrangement processes occur, and the shape of the $J = 1$ channel shows an attraction analogous to the $J = 2$ channel as calculated by the HAL QCD Collaboration; and (*b*) the $J = 1$ channel is completely dominated by strangeness-rearrangement processes—that is, a complete absorption is assumed for this channel. The correlation functions that result from assumptions *a* and *b* are represented in **Figure 4*b*** by the orange and blue lines, respectively. For

both predictions, the Coulomb interaction is also taken into account, and the colored widths of the curves in **Figure 4*b*** represent the intrinsic uncertainties of the lattice QCD calculations, with the gray curves showing, in addition, the uncertainties related to the experimental determination of the source radius. Clearly, the most attractive solution is preferred by the data, although the calculations underpredict the ALICE results at all k^* values. In the absence of measurements of the $p\Omega^- \rightarrow \Xi\Lambda, \Xi\Sigma$ cross sections, future studies of $\Lambda\Xi^-$ and $\Sigma^0\Xi^-$ correlations will help reduce the uncertainties in the expectations from theory by pinning down the contributions of the inelastic channels.

An evident depletion is present in the lattice QCD predictions shown in **Figure 4*b***. By looking in particular to the region $k^* \in [100, 200]$ MeV/c, one can see that the correlation function reaches values below the Coulomb-only prediction. Such depletion, which is not confirmed by the experimental data, is due to the presence of the $p\Omega^-$ dibaryon state. The strength of the depletion depends on (*a*) the characteristics of the interaction, (*b*) the BE of the $p\Omega^-$ state, and (*c*) the size of the particle-emitting source. This dependence has been analyzed in detail in Reference 46 through the study of the interplay of the scattering length associated with the $p\Omega^-$ interaction and the corresponding correlation function obtained for different source sizes.

The ALICE data shown in **Figure 4*b*** do not follow the depletion predicted by the lattice QCD calculations. To obtain firm conclusions on the possible existence of the $p\Omega^-$ state and, if existent, to experimentally quantify its BE, a differential analysis of the $p\Omega^-$ correlations in systems with slightly different source sizes is necessary. This can be done at the LHC in the ALICE experiment by studying p+Pb and peripheral Pb+Pb collisions.

To show more clearly the effect of a possible bound state in the correlation function, it is useful to compare several local potentials describing the $p\Omega^-$ $J = 2$ interaction that either are associated with $p\Omega^-$ bound states with different properties or do not predict any bound state. We make use here of the potentials presented in Reference 93, labeled V_I, V_{II}, and V_{III}. These potentials are based on past calculations by the HAL QCD Collaboration with nonphysical quark masses ($m_\pi =$ 875 MeV, $m_K = 916$ MeV) (94). For the construction of the V_{II} potential, the lattice QCD data in Reference 94 are fitted by an attractive Gaussian core plus and attractive Yukawa tail, while for the V_I and V_{III} potentials the range parameter at long distance of the fit is varied to obtain a weaker and stronger attraction, respectively. The radial shape of such potentials compared with the most recent HAL QCD potential with physical quark masses ($m_\pi = 146$ MeV, $m_K = 525$ MeV) (46) can be seen in **Figure 5*a***. For V_I, no bound state is predicted; for V_{II}, a bound state with strong-only binding of 0.05 MeV and strong + Coulomb binding of 0.63 MeV is predicted; and for V_{III}, a bound state with strong-only binding of 24.8 MeV and strong + Coulomb binding of 26.9 MeV is predicted (93).

Figure 5*b* displays the corresponding correlation functions for a source with $r_0 = 0.95 \pm 0.06$ fm. One can compare the limiting case of a deeply bound $p\Omega^-$ state that has a BE of 24.8 MeV (V_{III} potential) with the case of a very shallow BE of 0.05 MeV (V_{II} potential) or no bound state (V_I potential). Although the V_I potential is much less attractive than the V_{III} at all distances, the correlation function of the former is higher because of the deep depletion caused in the latter by the presence of a deeply bound state. A comparison of the V_{II} and V_{III} curves shows the same effect; the shallow BE of the V_{II} potential is reflected in a much shallower depletion as well. The correlation function corresponding to the most recent HAL QCD potential with physical quark masses (46) is also shown. The BE of a few MeV is reflected in a correlation function that is lower than the one for the V_{II} potential even though the latter is less attractive for distances $r > 0.6$ fm. In general, a consistent picture is shown in which, for a very attractive interaction at all distances, the final correlation function for a small source size of around 1 fm is determined to a high degree from the predicted BE of the bound state and the depletion caused by it.

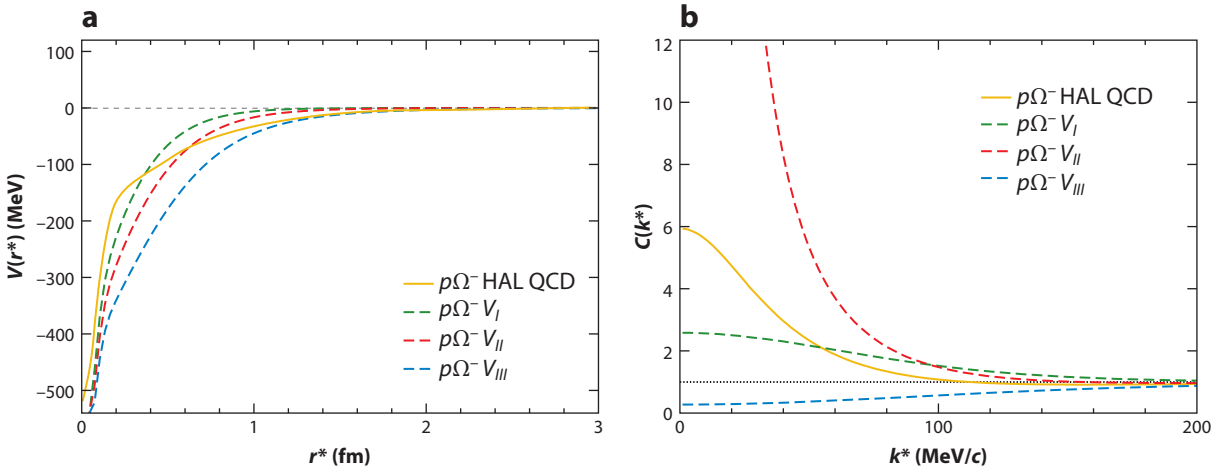

Figure 5

(*a*) Comparison of the strong interaction potentials for $p\Omega^-$ from Reference 93 (*dashed lines*) and Reference 46 (*solid orange line*). The potentials V_{II} (*red*) and V_{III} (*blue*) imply a $p\Omega^-$ bound state with binding energies due to strong interactions of 0.05 and 24.8 MeV. No bound state is associated with the V_I (*green*) potential. The solid orange line represents the HAL QCD potential with nearly physical quark masses (46) predicting a binding energy of 1.54 MeV. (*b*) Correlation functions for $p\Omega^-$ pairs corresponding to the potentials shown in panel *a* for a radius of 0.95 fm.

The correlation functions obtained from the V_I, V_{II}, and V_{III} potentials for source sizes ranging from 2 to 5 fm have been compared with data from ultrarelativistic Au+Au collisions at a center-of-mass energy of 200 GeV per nucleon pair by the STAR Collaboration (32). The combination of low purity and statistical significance of the data with such a large system size reduces the sensitivity of the comparison, as discussed at the end of Section 2. The ratio of the correlation function for $p\Omega^-$ pairs in peripheral collisions (centralities of 40–80%) to the one in central collisions (centralities of 0–40%) at $k^* = 20$ MeV/c is compatible within 1σ with the V_{III} and within 3σ with the V_I and V_{II} potentials for an expanding source.

4.3. Coupled-Channel Dynamics

Coupled-channel processes are widely present in hadron–hadron interactions whenever pairs of particles that are relatively close in mass share the same quantum numbers: baryonic charge (B), electric charge (Q), and strangeness (S). The coupling translates into on-/off-shell transitions from one system to the other.

Whenever present, the multichannel dynamics deeply affects the hadron–hadron interaction and is at the origin of several phenomena, such as bound states and resonances, which crucially depend on the coupling between these inelastic channels. A striking example can be found in the origin of the $\Lambda(1405)$, a molecular state that arises from the coupling of an antikaon–nucleon ($\bar{K}N$) to $\Sigma\pi$ (95, 96). In the baryon–baryon sector, the coupling between $N\Lambda$ and $N\Sigma$ is of great importance in providing the repulsive behavior of Λ hyperons in dense nuclear matter (70). Since in femtoscopic measurements the final state is fixed (the measured particle pair), the corresponding correlation function represents an inclusive quantity that can show sensitivity to all the available initial inelastic channels produced in the collision (77, 97).

The effect of coupled channels on the final measured correlation function depends on two main ingredients: the coupling constant strength stemming from the strong multichannel dynamics,

and the conversion weights—namely, the number of pairs in the corresponding channel produced close enough to convert into the final measured state. The correlation function in Equation 1 needs to be modified, and for a system with N coupled channels, this observable in the i channel that is measured reads (44, 77, 97)

$$C_i(k^*) = \int \mathrm{d}^3 r^* S_i(r^*) |\psi_i(k_i^*, r^*)|^2 + \sum_{j \neq i}^{N} w_j \int \mathrm{d}^3 r^* S_j(r^*) |\psi_j(k_j^{*'}, r^*)|^2. \quad 10.$$

Generally speaking, the emitting source $S_i(r^*)$ and the one for the incoming inelastic channels, $S_j(r^*)$, might be different (since the m_T distribution of the different pairs can differ), but the results presented in Section 3 and the proximity in mass among the different channels quantitatively prove that the equality $S_i(r^*) = S_j(r^*)$ can be assumed.

The first integral on the right-hand side of Equation 10 describes the elastic contribution where initial and final state coincide, while the second integral is responsible for the remaining inelastic processes $j \rightarrow i$. The last integral depends on two main ingredients: the wave function $\psi_j(k_j^*, r^*)$ for channel j going to the final state i and the conversion weights w_j. The latter are directly related to the number of pairs, for each inelastic channel, produced in the initial collision that are kinematically available to convert into the final measured state. Estimates for these weights can be obtained using information on yields from statistical hadronization models (63–65) and on the kinematics of the produced pairs from transport models (66).

As can be seen from Equation 10, the correlation function involves contributions from both elastic and inelastic components, and in principle, the scattering amplitude of the single-channel i cannot be fully isolated from the inelastic contributions. Depending on the coupling strength, the coupled-channel contributions j modify the $C(k^*)$ in two different ways based on whether their opening (the minimum energy at which they can be produced) occurs below or above the production threshold of the considered pair (the reduced mass of the pair). Inelastic channels that open below threshold do not introduce any shape modification to the $C(k^*)$; rather, they act simply as an effective attraction, increasing the signal strength of the correlation function. Channels that appear above threshold instead lead to a modification of the k^* dependence of the $C(k^*)$ in the vicinity of the opening, which is typically translated into a cusp structure whose height is driven by the coupling strength.

These two main differences are illustrated in **Figure 6** for the K^-p and $p\Lambda$ systems. The K^-p system presents couplings to several inelastic channels below threshold, such as $\pi\Lambda$ and $\pi\Sigma$, and, due to the breaking of isospin symmetry, to charge-conjugated $\bar{K}^0 N$ at roughly 4 MeV above threshold corresponding to $k^* \approx 60$ MeV/c in the $C(k^*)$. **Figure 6*a*** shows a schematic representation of the collision. From the emitting source formed after the collision, all the pairs constituting the four coupled channels are produced and described by the corresponding wave functions $\psi_j(k_j^*, r^*)$. The correlation of K^-p pairs composing the final state (channel 1) is measured (**Figure 6*b***), and the decomposition in the different channels' contributions is shown in **Figure 6*c*,*d*** for two different source sizes. The largest contributions to the $C(k^*)$ from coupled channels occur for a small emitting source with $r_\mathrm{G} = 1$ fm (**Figure 6*c***). The $C(k^*)$ signal increases as the inelastic contributions are added, and the cusp structure, which is visible when the $\bar{K}^0 n$ channel is explicitly added, indicates the opening of this channel above threshold. For both source radii, this structure already appears when the mass difference between K^- and $\bar{K}^0$ is considered, and it is also present in the elastic $K^-p \rightarrow K^-p$ contribution. As mentioned above, the explicit inclusion of the $\bar{K}^0 N$ contribution acts as an "effective" attraction component, increasing the signal of the correlation function and of the cusp according to the strength of the coupling between the two channels. This effect is suppressed when the source size is increased up to $r_\mathrm{G} =$ 4 fm (**Figure 6*d***), as in central HICs.

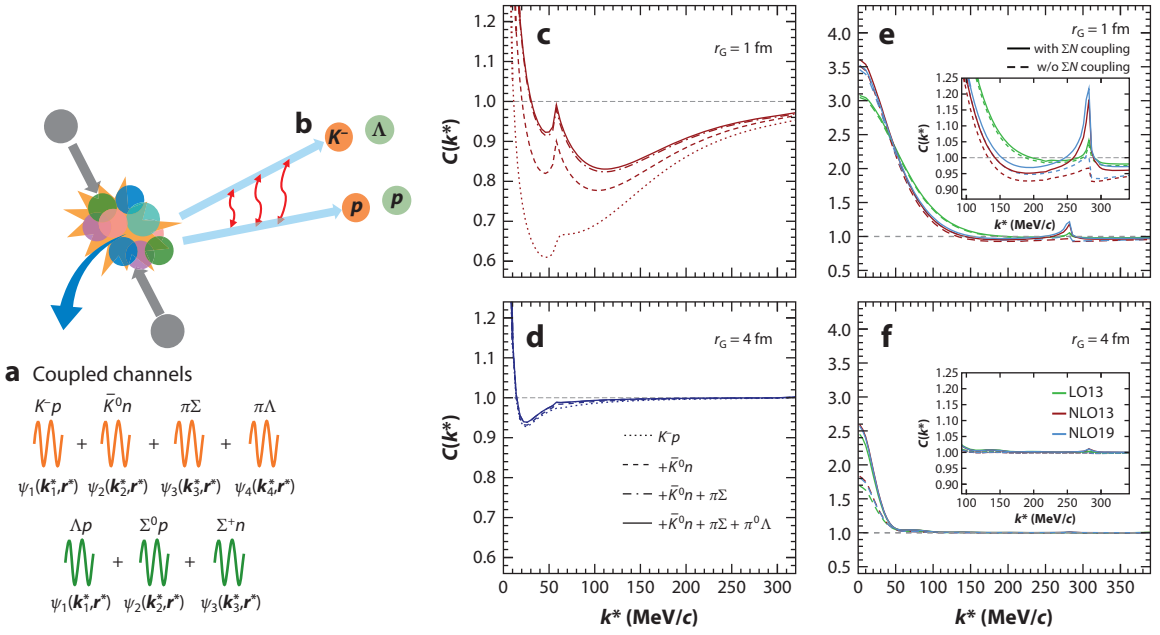

Figure 6

Schematic representation of the effects of coupled channels on the K^-p and $p\Lambda$ correlation function. (*a*,*b*) System configuration in femtoscopic measurements, where only the final K^-p and $p\Lambda$ channels are measured. The upper panels (*c*,*e*) on the right show results for radii achieved in *pp* collisions (1 fm). The lower panels (*d*,*f*) on the right show results for radii achieved in heavy-ion collisions (4 fm). Panels *c* and *d* show the correlation functions for K^-p from the pure elastic term (*dotted line*) to the full $C(k^*)$ (*solid line*) with all coupled channels ($\bar{K}^0n$, $\pi\Sigma$, $\pi\Lambda$) included and the conversion weights fixed to unity. Panels *e* and *f* show the $p\Lambda$ correlation functions obtained assuming LO [LO13 (69)] and two versions of NLO [NLO13 (69), NLO19 (70)] chiral effective field theory calculations. Contributions from *S*-, *P*-, and *D*-waves are included. Dashed lines indicate results with only the elastic term $p\Lambda \rightarrow p\Lambda$ in Equation 10. Solid lines indicate results with the inclusion of coupled-channel contributions in Equation 10 from $n\Sigma^+$ and $p\Sigma^0$ with conversion weight 1/3. Abbreviations: LO, leading order; NLO, next-to-leading order.

A similar trend can be seen when another strongly coupled channel is introduced: the $\pi\Sigma$ (see dashed–dotted line in **Figure 6*c***), which is responsible for the dynamic generation of the molecular state $\Lambda(1405)$. The strong coupling to this channel, lying below threshold, is directly translated into the correlation function of K^-p pairs and is visible as a clear enhancement of the signal at low momentum with respect to the single-channel contribution.

The extreme sensitivity to coupled-channel contributions of the $C(k^*)$ obtained in small systems has been confirmed recently by results for the K^-p correlation function, measured by the ALICE Collaboration in *pp* collisions at different energies (38). Future measurements of this pair, performed in different colliding systems, will also provide quantitative constraints on the coupling strength to the $\bar{K}^0n$ channel.

In **Figure 6*e*,*f***, another coupled system, which is formed by the interaction of a Λ and a Σ with nucleons, is depicted. The strength in the $N\Lambda \leftrightarrow N\Sigma$ conversion is not experimentally well constrained since scattering measurements cannot currently provide precise enough data on the $p\Lambda$ cross section at momenta close to the opening (5–7). The only experimental observations of the Σp cusp have been extracted in partial-wave analyses of $pp \rightarrow pK^+\Lambda$ reactions at low energy, but they are strongly affected by Λp final-state interactions (98, 99).

In **Figure 6*e***, the theoretical $p\Lambda$ correlation function obtained with different calculations based on χEFT at NLO (69, 70) and LO (69) is shown for a source radius of 1 fm and for a momentum

cutoff parameter of 600 MeV/c. The coupling to the $N\Sigma$ ($n\Sigma^+$, $p\Sigma^0$) occurs already in the S-wave and finds the largest contribution from D-waves; hence, partial waves up to $l = 2$ are included. The conversion weights w_j for this coupling in Equation 10 can be fixed to 1/3 from isospin symmetry, a value comparable to thermal model calculations (63) and measurements of production ratios between these two hadrons at high energies (100, 101). The inclusion of the $N\Sigma$ coupled-channel contributions, as shown for the K^-p case, leads to the appearance of a cusp structure at $k^* =$ 289 MeV/c, which corresponds to the kinematic opening of the inelastic $n\Sigma^+$ and $p\Sigma^0$ channels. The low-momentum region of the $C(k^*)$ is not deeply affected by the explicit inclusion of the inelastic terms since the opening of the $N\Sigma$ occurs above threshold.

The largest differences in the behavior of the $C(k^*)$, regardless of the presence or absence of $N\Sigma$ contributions, arise in the LO and NLO descriptions. The LO predictions have already been ruled out by scattering data in the proximity of the cusp region since the calculation deviates significantly from the data despite the large uncertainties. The two versions of the NLO calculations (NLO13, NLO19) differ mainly in the description and strength of the $\Lambda \leftrightarrow \Sigma$ conversion potential, which leads to significant modifications of the Λ hyperon interaction in dense nuclear matter and to different results for light hypernuclei.

As can be seen in **Figure 6**, the cusp height predicted from these two approaches is similar, but mild differences are present below and above the cusp. The high-precision data delivered by the recent ALICE measurements on $p\Lambda$ pairs (102) favor the latest NLO19 chiral potential, indicating a weak coupling between N–Λ and N–Σ channels and predicting a more attractive Λ single-particle potential in neutron matter. This current picture regarding the $p\Lambda$ interaction has profound implications for three-body hyperonic forces. This scenario is also directly relevant to open problems in astrophysics, such as the presence of hyperons in NSs (9, 10, 103).

In conclusion, femtoscopic measurements in pp collisions are able to probe the short-distance region of the pair wave function, in which the coupled-channel dynamics dominates the strong interaction. Moving to larger source sizes tests the asymptotic part of the wave function where the inelastic terms are noticeably suppressed and partial access to the pure elastic interaction can be obtained. This makes it possible to investigate the dynamics of the couplings between the elastic and inelastic channels by performing femtoscopic measurements of the same pair in different colliding systems, which might lead to a complete description of all hadron–hadron interactions within SU(3).

5. IMPLICATIONS FOR NEUTRON STARS

Knowledge regarding the interaction of hyperons with nucleons is one of the key ingredients needed to understand the composition of the most dense objects in our universe: NSs (104, 105). These kinds of stars are the final outcome of supernova explosions and are typically characterized by large masses ($M \approx 1.2$–$2.2 M_\odot$) and small radii ($R \approx 9$–13 km) (106–108). In the standard scenario, the gravitational pressure is typically counterbalanced by the Fermi pressure of neutrons in the core, which, along with electrons, are the only remnants from the mother star collapse. The high-density environment ($\rho \approx 3$–$4\rho_0$) that is supposed to occur in the interior of NSs leads to an increase in the Fermi energy of the nucleons, translating into the appearance of new degrees of freedom, such as hyperons. This energetically favored production of strange hadrons induces a softening of the EoS. The behavior of the mass as a function of the radius has a unique correspondence with the EoS through the solution of the Tolman–Oppenheimer–Volkoff equations; hence, the mass–radius relation strongly depends on the constituents of the EoS and on their interactions. The inclusion of hyperons leads to NS configurations that cannot reach the current highest mass limit from experimental observations of $2.2 M_\odot$ (108). For this reason, the presence

of hyperons inside the inner cores of NSs is still under debate, and this so-called hyperon puzzle is far from being solved (109, 110).

A key element in the complete understanding of this puzzle is the interaction of hyperons with the surrounding medium, which strongly affects the properties of the corresponding EoS (8, 111) and can be related to the interaction between hyperons and nucleons (*YN* and *YNN*) in vacuum. A repulsive *YN* interaction occurring already at the two-body level can push the appearance of hyperons to larger densities, limiting the possible presence of these particle species inside NSs, stiffening the EoS, and allowing for larger star masses.

The more precisely the hyperon–nucleon two-body and three-body interactions are known in vacuum, the more detailed the knowledge of the hyperonic content inside NSs will be. Much interest in this topic has been triggered by the recent measurements of gravitational wave signals from NS mergers, which opened a new gate through which to experimentally access the properties of the matter inside NSs.

As shown in the sections above, femtoscopy can provide new insight into interactions involving nucleons and hyperons that are poorly understood or not accessible with scattering experiments. A key example is given by the femtoscopic measurements of the $p\Lambda$ strong interaction. Because of their light mass, the Λ baryons are typically the first hyperon species produced inside NSs. Their appearance is also theoretically favored by the overall attractive potential that a Λ feels at the saturation density, $U_\Lambda = -30$ MeV (68). The results obtained on this system, as discussed in Section 4.3, support recent χEFT calculations in which an even more attractive interaction of the Λ with the surrounding nucleons, due to the $\Lambda N \leftrightarrow \Sigma N$ dynamics, is predicted. In this case, the early appearance of Λ hyperons in neutron matter will lead to an overly soft EoS and ultimately to stable light NS configurations. To coexist with the astrophysical constraints on NS masses, such a scenario requires the introduction of repulsive forces that might be present in other *YN* systems and in the inclusion of three-body interactions.

Repulsive hyperon–nucleon–nucleon interactions, such as ΛNN, have already been included in several approaches to obtain a stiffer EoS (9, 112). However, at the moment, these three-body forces rely on the experimental measurements of hypernuclei BEs ($^4_\Lambda$H, $^4_\Lambda$He), in which the determination of the genuine ΛNN interaction is not straightforward and can be affected by many-body effects. For this reason, the current theoretical understanding of the role played by three-body terms in the strangeness $|S| = 1$ sector inside NSs is not yet settled.

A major advance in understanding the role played by heavier strange hadrons in the hyperon puzzle has been achieved by the validation of lattice QCD predictions for the $N\Xi$ interaction. As shown in Section 4.1, the measurement of the $p\Xi^-$ correlation (41) confirmed a strong attractive interaction between these two hadrons and provided a direct confirmation of lattice potentials (75). Using this same interaction as a starting point to extrapolate results in a neutron-rich dense system, one can obtain a repulsive average interaction of roughly +6 MeV (113). Currently, models for EoSs that include Ξ hyperons assume large variations in the values of the single-particle potential (-40, $+40$ MeV) (8), and hence the validated lattice predictions impose a much more stringent constraint. **Figure 7*a*** shows the fractions [obtained from mean-field calculations (8, 111, 114, 115; D. Chatterjee, S. Gosh, J. Schaffner-Bielich, manuscript in preparation)] of particles produced in the inner part of NSs as a function of the energy density. The single-particle potentials for Λ and Σ hyperons have been fixed to the current values constrained from scattering data and hypernuclei and confirmed by the LHC measurements.

The isovector couplings to the Ξ have been adjusted to reproduce the predicted results in pure neutron matter obtained from HAL QCD calculations at finite density (113), stemming from the predictions in vacuum discussed in Section 4.1. The slight repulsion acquired by a Ξ^- in pure neutron matter directly translates into larger energy densities, and hence larger nuclear densities,

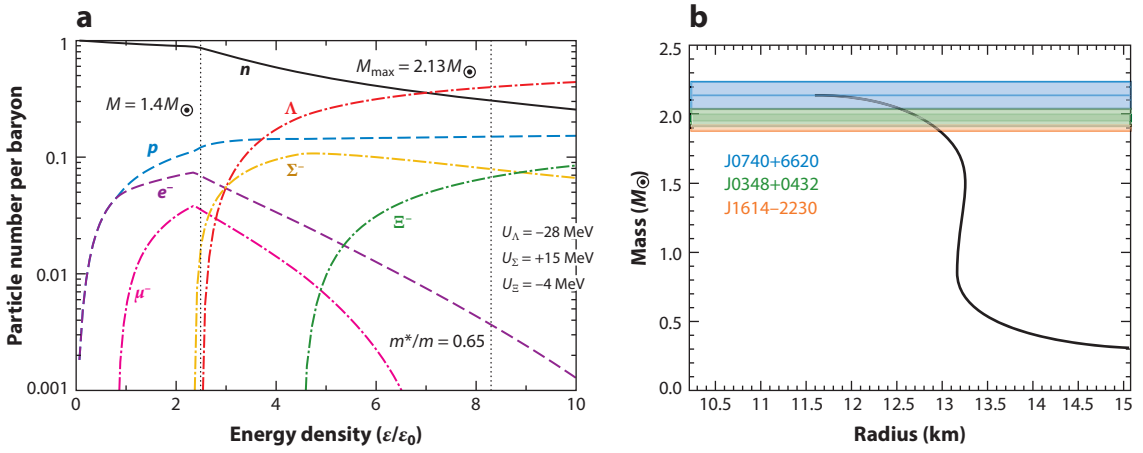

Figure 7

(*a*) Fraction of particles produced in the inner core of a neutron star as a function of the energy density, in units of energy density ε_0 at the nuclear saturation point. The single-particle potential depths in symmetric nuclear matter for Λ, Σ, and Ξ hyperons are displayed. The vertical dotted lines indicate the central energy densities reached for a standard neutron star of $1.4M_\odot$ and for the maximum mass, $2.13M_\odot$, reached within this specific equation of state. The mean-field calculations (8, 111, 114, 115) have been tuned to reproduce the lattice predicted value of U_Ξ in pure neutron matter obtained in Reference 113, using the in-vacuum results validated by ALICE data in Reference 41. The equation of state obtained with these constraints provides a stable neutron star with a maximum mass of $M_{\rm max} = 2.13M_\odot$, as seen in the mass–radius plot in panel *b*, and is compatible with recent astrophysical measurements of heavy neutron stars, indicated by the orange (106), green (107), and blue (108) bands in panel *b*.

for the appearance of this hyperon species. **Figure 7*b*** shows the resulting mass–radius relation obtained by assuming the predicted HAL QCD Ξ interaction in medium. The production of cascade hyperons that occurs at higher densities leads to a maximum NS mass of $2.13M_\odot$, which is fully compatible with the recent measurements of NSs close to and above two solar masses (106–108).

Recent results in small colliding systems have proved that femtoscopy can play a central role in understanding the dynamics among hyperons and nucleons in vacuum. Comparisons between hadronic models and these data are necessary to constrain calculations at finite density and to pin down the behavior of hyperons in a dense matter environment. The unique possibility of investigating different *YN* interactions and extending the measurements to three-body forces may finally provide quantitative input to the long-standing hyperon puzzle.

6. OUTLOOK

A complete program of new measurements in *pp* collisions at 14 TeV has been approved for the upcoming Runs 3 and 4 of the LHC with ALICE (116). To address further questions regarding two- and three-body forces that involve hyperons, correlation studies constitute one of the main foci of such a program. Studies will benefit from data taking with increased instantaneous luminosity and readout speed, plus better tracking and vertexing performance of the upgraded apparatus. Moreover, the new data acquisition system will make it possible to select events with very high multiplicity, up to 16 times the average multiplicity of minimum-bias *pp* collisions. Accessing such a regime of multiplicities in *pp* events is particularly beneficial for measurements including strange hadrons because of the enhanced production of strangeness in collisions with high multiplicity (53). Assuming an acquired luminosity of 200 pb^{-1} and a selection of events with a number of produced charged particles ($N_{\rm ch}$) seven times higher than the mean number of charged particles

in minimum-bias collisions, $N_{ch} > 7\ \langle N_{ch} \rangle$, an overall increase up to a factor of 50 for particle pairs per event is expected for the Run 3 high-multiplicity data with respect to the sample collected in Run 2 (116).

Several new analyses can be performed with the Run 3 and Run 4 data that were not possible with the Run 1 and Run 2 statistics, and the question of three-body forces including hyperons can finally be addressed experimentally.

6.1. K^-d Correlations

Following the measurement of K^-p correlations in pp collisions (38), the study of the correlation function of K^-d pairs will be realized. Together with the planned measurements at threshold using kaonic atoms by SIDDHARTA-2 (117), the K^-d femtoscopy will allow us to determine for the first time the full isospin dependence of the $\overline{K}N$ interaction, a fundamental problem in the strangeness sector in the low-energy regime of QCD.

6.2. $p\Sigma^0$ Correlations

Investigation of the $p\Sigma^0$ correlation will provide precise data on an interaction that, in contrast to the $N\Lambda$ interaction, is currently very poorly known experimentally. A first measurement (39) of this correlation was performed using high-multiplicity pp collisions and demonstrated the feasibility of the approach, although with large statistical uncertainties and relatively low signal purity. The minimum-bias pp Run 3 data will allow a yield of $p\Sigma^0$ pairs 10 times higher than in the Run 2 data, which will deliver the first precise data in the field. At the same time, lattice QCD calculations are expected to reach precision in the $|S| = 1$ sector within the next few years, and hence the new measurement can contribute to the validation of the state-of-the-art theoretical calculations.

6.3. $\Lambda\Xi$ Correlations

The enhancement of the yield of strange particles in the high-multiplicity data from Run 3 will allow us to study the $\Lambda\Xi$ interaction with high precision. Such a study will complement the measurements of $p\Omega^-$ correlations, and their comparison to the lattice QCD calculations. For the $p\Omega^-$ interaction, the $J = 1$ channel lacks any prediction so far since it is dominated by absorption in the $\Lambda\Xi$ and $\Sigma\Xi$ channels. The study of the $\Lambda\Xi$ will hence provide the first experimental constraints to the contribution of the coupled channels for the $p\Omega^-$ system.

6.4. $\Omega\Omega$ Correlations

The HAL QCD Collaboration has provided lattice QCD calculations at the physical point for the $\Omega\Omega$ system, which predict the existence of "the most strange dibaryon" with a BE of around 1.6 MeV (118), as implied by the strong attractive character of the $\Omega\Omega$ strong interaction and by the fact that the Pauli principle does not apply for this system.

So far, no experimental data are available for this interaction. The measurement of the $\Omega\Omega$ correlation function is extremely challenging and is constantly requested by theoreticians. During Run 3, the data acquisition of the ALICE experiment will be implemented with a dedicated trigger for Ω decays that can sample the whole 200 pb^{-1} of the pp data taking, resulting in a total of 2×10^9 reconstructed and recorded $\Omega^- \oplus \Omega^+$. For the correlation studies, about 500 $\Omega\Omega$ pairs are expected to be reconstructed with low relative momentum ($k^* < 200$ MeV/c).

On the theoretical side, the predictions from the HAL QCD Collaboration (46) provide the $^1S_0$ channel of the $\Omega\Omega$ interaction alone. This is the channel with the smallest contribution (weight

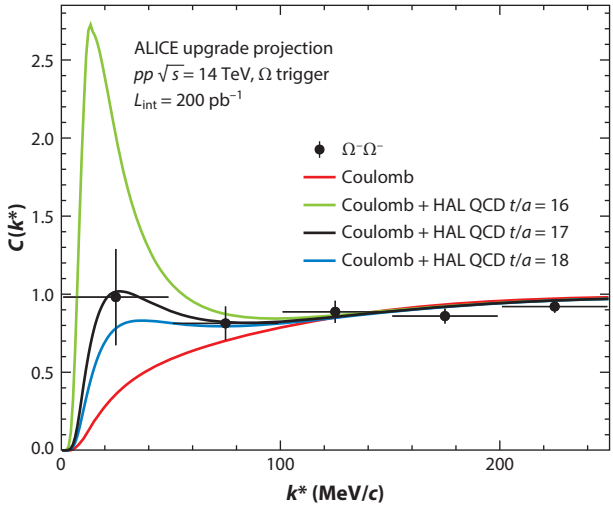

Figure 8

Expected precision of the ΩΩ correlation function with ALICE Run 3 data (*black points*). The red curve represents the Coulomb-only scenario, and the green, black, and blue lines indicate the strong interaction potentials predicted by the HAL QCD Collaboration for different integration times ($t/a = 16$, 17, and 18, respectively). The Gaussian source used for the calculations has a radius of $r = 0.8$ fm. The simulated data follow the Coulomb + HAL QCD $t/a = 17$ scenario.

1/16), and an attractive interaction is also expected for the $^5S_2$ channel (weight 5/16), but the calculations are not available yet.

Figure 8 shows a projection of the measurement of the ΩΩ correlation compared with the Coulomb-only scenario and three different curves with the additional strong interaction predicted by the HAL QCD Collaboration. One can see that for the lattice calculations ($^1S_0$ channel), there are substantial differences in the expected correlation function considering different integration times (t/a parameter). This is true in particular for a very small source like the one expected for ΩΩ pairs in *pp* collisions, with a radius of around $r = 0.8$ fm.

A precision of 31% at $k^* = 25$ MeV/c is expected in the correlation function using a bin width of 50 MeV/c. This would constitute a groundbreaking measurement of the ΩΩ interaction; it would provide the first constraint on the lattice QCD calculations and the potential to experimentally determine, for the first time ever, the sign of the strong interaction between ΩΩ pairs.

6.5. Λ*d* Correlations

Complementing the studies of Λ*p* correlations, the study of the Λ*d* correlation function provides additional information on the Λ*N* interaction. Experimental access to information on direct Λ*d* scattering is even harder to obtain than that from Λ*p* scattering, and correlation studies will constitute an additional and independent source of information for this channel. Moreover, the measurement of the Λ*d* correlation function in small systems complements the measurement of the hypertriton BE and delivers information on many-body forces (119).

There are two different spin configurations in the *S*-wave Λ*d* interaction: the doublet $^2S_{1/2}$ and the quartet $^4S_{3/2}$ states. With no scattering data available for the Λ*d* channel, the scattering parameters in the doublet state are constrained by measurements of the lifetime of the bound state found in this partial wave: the hypertriton, $^3\mathrm{H}_\Lambda$. The hypertriton BE is related to the scattering

parameters in the effective range approximation via the Bethe formula (120). The higher spin configurations are not binding, and they are currently not tested by any experimental data. For the constraint of the quartet state, chiral SU(3) calculations (121) have been used so far.

The expected precision of the measurement of the Λd correlation function with the *pp* high-multiplicity data sample with $N_{\rm ch} > 7\ \langle N_{\rm ch} \rangle$ during Run 3 at $k^* = 50$ MeV/c is on the order of 5% (with a bin width of 20 MeV/c). Such a precise measurement will complement the hypertriton BE measurements, scanning the full spin dependence of the Λ interaction and, as has been suggested, possibly providing insight into the coalescence process. These studies in *pp* collisions can be complemented by studies in larger systems (Pb+Pb) and lead to better knowledge and understanding of many-body forces acting in light hypernuclei (119).

6.6. Three-Body Forces

In addition to the Λd measurement, the study of three-body interactions involving hyperons, which are extremely important in understanding the structure of NSs, will be experimentally accessible with high precision for the first time. Exclusive measurements of $pp\Lambda$ and correlations with a newly developed mathematical formalism using cumulants that allow the study of the correlation function of three particles with nonidentical masses will enable one to access the final-state interaction. For this purpose, the data acquisition will be implemented to sample the whole data taking, recording events where at least two proton candidates and one Λ candidate are reconstructed using an online trigger selection.

7. SUMMARY

The correlation technique employed to study the strong interaction among hadrons has been discussed. Since a precise understanding of the source that characterizes the particle emission is mandatory to extract the strong interaction from correlations, a dedicated model for small colliding systems at the LHC has been motivated and explained. In this formulation, the contribution from the strong decay of short-lived resonances has been modeled, and the hypothesis of a universal source for all hadron–hadron pairs has been demonstrated and exploited in all the discussed analyses. The method has been tested employing *pp* and $p\Lambda$ correlations, where the interaction is rather well known, especially for *pp* pairs. Following this scheme, the results achieved for several hyperon–nucleon, hyperon–hyperon, and kaon–nucleon combinations have been presented. The first measurement of the attractive $p\Xi^-$ strong interaction was presented and confirmed by lattice calculations by the HAL QCD Collaboration. The precise measurement of the $\Lambda\Lambda$ interaction has allowed for extraction of the most precise upper limit for the BE of a possible *H* dibaryon state. The first measurement of the attractive strong $p\Omega^-$ interaction has been shown as well. In the latter case, the results compared with lattice calculations for the first time do not show any clear evidence for the existence of a bound state. It has been shown that the presence of the coupled-channel dynamics in the K^-p and $p\Lambda$ channels manifests itself on the correlation functions. The couplings $\bar{K}^0 N \leftrightarrow K^- p$ and $N\Lambda \leftrightarrow N\Sigma$ have been directly observed for the first time.

The consequences of the new measurement of the strong interaction among protons and strange hadrons for the physics of NSs have also been addressed. The example related to the Ξ^- strong interaction has shown the impact of the new measurements on astrophysics. The measurement of additional two-body correlations and possibly three-body correlations among hyperons and nucleons is planned for the future and, if achieved, will impose more stringent constraints for NSs. In particular, the physics opportunities that will be available during the LHC Run 3 data taking have been sketched above.

In general, the correlation technique applied to small colliding systems at the LHC is a promising tool with which to investigate the strong interactions. For this reason, a new laboratory to study hadron–hadron interactions has been established with the capability to unveil the strong interaction among any hadron–hadron pair.

DISCLOSURE STATEMENT

The authors are not aware of any affiliations, memberships, funding, or financial holdings that might be perceived as affecting the objectivity of this review.

ACKNOWLEDGMENTS

The authors would like to thank Dimitar Mihaylov, Alice Ohlson, and Thomas Humanic for their input and comments regarding this manuscript. Special thanks also to Juergen Schaffner-Bielich, Debarati Chatterjee, Suprovo Gosh, and Benjamin Doenigus for the interesting discussions on neutron star physics. This work was supported by DFG EXC 2094 390783311 ORIGINS, GSI TMLRG1316F, BmBF 05P15WOFCA, SFB 1258, and DFG FAB898/2-2.

LITERATURE CITED

1. Arndt R, Briscoe W, Strakovsky I, Workman R. *Phys. Rev. C* 76:025209 (2007)
2. Navarro Pérez R, Amaro J, Ruiz Arriola E. *Phys. Rev. C* 88:024002 (2013). Erratum. *Phys. Rev. C* 88:069902 (2013)
3. Mast TS, et al. *Phys. Rev. D* 14:13 (1976)
4. Ciborowski J, et al. *J. Phys. G* 8:13 (1982)
5. Eisele F, et al. *Phys. Lett. B* 37:204 (1971)
6. Alexander G, et al. *Phys. Rev.* 173:1452 (1968)
7. Sechi-Zorn B, Kehoe B, Twitty J, Burnstein R. *Phys. Rev.* 175:1735 (1968)
8. Weissenborn S, Chatterjee D, Schaffner-Bielich J. *Nucl. Phys. A* 881:62 (2012)
9. Lonardoni D, Lovato A, Gandolfi S, Pederiva F. *Phys. Rev. Lett.* 114:092301 (2015)
10. Gerstung D, Kaiser N, Weise W. *Eur. Phys. J. A* 56:175 (2020)
11. Hanbury Brown R, Twiss R. *Nature* 178:1046 (1956)
12. Goldhaber G, Goldhaber S, Lee W, Pais A. *Phys. Rev.* 120:300 (1960)
13. Gyulassy M, Kauffmann SK, Wilson LW. *Phys. Rev. C* 20:2267 (1979)
14. Zajc WA, et al. *Phys. Rev. C* 29:2173 (1984)
15. Fung SY, et al. *Phys. Rev. Lett.* 41:1592 (1978)
16. Wiedemann UA, Heinz UW. *Phys. Rep.* 319:145 (1999)
17. Podgoretsky M. *Fiz. Elem. Chast. Atom. Yadra* 20:628 (1989)
18. Adamczewski-Musch J, et al. *Phys. Rev. C* 94:025201 (2016)
19. Agakishiev G, et al. *Phys. Rev. C* 82:021901 (2010)
20. Abbott T, et al. *Phys. Rev. Lett.* 69:1030 (1992)
21. Barrette J, et al. *Phys. Lett. B* 333:33 (1994)
22. Bamberger A, et al. *Z. Phys. C* 38:79 (1988)
23. Bamberger A, et al. *Phys. Lett. B* 203:320 (1988)
24. Heinz UW, Kolb PF. Two RHIC puzzles: early thermalization and the HBT problem. In *Proceedings of the 18th Winter Workshop on Nuclear Dynamics*, ed. R Bellwied, J Harris, W Bauer, pp. 205–16. Debrecen, Hung.: EP Systema (2002)
25. Khachatryan V, et al. *Phys. Rev. Lett.* 105:032001 (2010)
26. Chojnacki M, Kisiel A, Florkowski W, Broniowski W. *Comput. Phys. Commun.* 183:746 (2012)
27. Adam J, et al. *Phys. Rev. C* 92:054908 (2015)
28. Lednický R. *Phys. Atom. Nucl.* 67:72 (2004)
29. Shapoval VM, Erazmus B, Lednicky R, Sinyukov YM. *Phys. Rev. C* 92:034910 (2015)

30. Adamczyk L, et al. *Phys. Rev. Lett.* 114:022301 (2015)
31. Adamczyk L, et al. *Nature* 527:345 (2015)
32. Adam J, et al. *Phys. Lett. B* 790:490 (2019)
33. Lisa MA, Pratt S, Soltz R, Wiedemann U. *Annu. Rev. Nucl. Part. Sci.* 55:357 (2005)
34. Morita K, Furumoto T, Ohnishi A. *Phys. Rev. C* 91:024916 (2015)
35. Acharya S, et al. arXiv:2005.11124 [nucl-ex] (2020)
36. Acharya S, et al. *Phys. Lett. B* 802:135223 (2020)
37. Acharya S, et al. *Phys. Rev. C* 99:024001 (2019)
38. Acharya S, et al. *Phys. Rev. Lett.* 124:092301 (2020)
39. Acharya S, et al. *Phys. Lett. B* 805:135419 (2020)
40. Acharya S, et al. *Phys. Lett. B* 797:134822 (2019)
41. Acharya S, et al. *Phys. Rev. Lett.* 123:112002 (2019)
42. Acharya S, et al. *Nature* 588:232 (2020)
43. Pratt S. *Phys. Rev. D* 33:1314 (1986)
44. Lednický R, Lyuboshitz V. *Sov. J. Nucl. Phys.* 35:770 (1982)
45. Mihaylov D, et al. *Eur. Phys. J. C* 78:394 (2018)
46. Morita K, et al. *Phys. Rev. C* 101:015201 (2020)
47. Acharya S, et al. *Phys. Rev. C* 96:064613 (2017)
48. Lisa MA, Pratt S. arXiv:0811.1352 [nucl-ex] (2009)
49. Bearden I, et al. *Eur. Phys. J. C* 18:317 (2000)
50. Adam J, et al. *Phys. Rev. C* 92:054908 (2015)
51. Khachatryan V, et al. *Phys. Lett. B* 765:193 (2017)
52. Khachatryan V, et al. *J. High Energy Phys.* 1009:91 (2010)
53. Adam J, et al. *Nat. Phys.* 13:535 (2017)
54. Acharya S, et al. *Phys. Rev. C* 99:024906 (2019)
55. Sirunyan AM, et al. *Phys. Rev. C* 97:064912 (2018)
56. Aad G, et al. *Eur. Phys. J. C* 75:466 (2015)
57. Abelev B, et al. *Phys. Rev. D* 87:052016 (2013)
58. Abelev B, et al. *Phys. Lett. B* 717:151 (2012)
59. Sirunyan AM, et al. *J. High Energy Phys.* 2003:14 (2020)
60. Acharya S, et al. *Phys. Lett. B* 811:135849 (2020)
61. Sinyukov Y, Shapoval V, Naboka V. *Nucl. Phys. A* 946:227 (2016)
62. Wiedemann UA, Heinz UW. *Phys. Rev. C* 56:3265 (1997)
63. Vovchenko V, Stoecker H. *Comput. Phys. Commun.* 244:295 (2019)
64. Becattini F, Passaleva G. *Eur. Phys. J. C* 23:551 (2002)
65. Wheaton S, Cleymans J. *Comput. Phys. Commun.* 180:84 (2009)
66. Pierog T, et al. *Phys. Rev. C* 92:034906 (2015)
67. Wiringa RB, Stoks V, Schiavilla R. *Phys. Rev. C* 51:38 (1995)
68. Hashimoto O, Tamura H. *Prog. Part. Nucl. Phys.* 57:564 (2006)
69. Polinder H, Haidenbauer J, Meißner UG. *Nucl. Phys. A* 779:244 (2006)
70. Haidenbauer J, Meißner UG, Nogga A. *Eur. Phys. J. A* 56:91 (2020)
71. Humphrey WE, Ross RR. *Phys. Rev.* 127:1305 (1962)
72. Watson MB, Ferro-Luzzi M, Tripp RD. *Phys. Rev.* 131:2248 (1963)
73. Nowak RJ, et al. *Nucl. Phys. B* 139:61 (1978)
74. Hadjimichef D, Haidenbauer J, Krein G. *Phys. Rev. C* 66:055214 (2002)
75. Sasaki K, et al. *Nucl. Phys. A* 998:121737 (2020)
76. Acharya S, et al. *Phys. Rev. Lett.* 123:112002 (2019)
77. Haidenbauer J. *Nucl. Phys. A* 981:1 (2019)
78. Takahashi H, et al. *Phys. Rev. Lett.* 87:212502 (2001)
79. Jaffe RL. *Phys. Rev. Lett.* 38:195 (1977). Erratum. *Phys. Rev. Lett.* 38:617 (1977)
80. Adam J, et al. *Phys. Lett. B* 752:267 (2016)
81. Ohnishi A, Morita K, Miyahara K, Hyodo T. *Nucl. Phys. A* 954:294 (2016)

82. Adamczyk L, et al. *Phys. Rev. Lett.* 114:022301 (2015)
83. Press WH, Teukolsky SA, Vetterling WT, Flannery BP. *Numerical Recipes: The Art of Scientific Computing*. New York: Cambridge Univ. Press. 3rd ed. (2007)
84. Ueda T, et al. *Prog. Theor. Phys.* 99:891 (1998)
85. Nagels MM, Rijken TA, de Swart JJ. *Phys. Rev. D* 15:2547 (1977)
86. Nagels MM, Rijken TA, de Swart JJ. *Phys. Rev. D* 20:1633 (1979)
87. Rijken TA, Nagels MM, Yamamoto Y. *Prog. Theor. Phys. Suppl.* 185:14 (2010)
88. Filikhin I, Gal A. *Nucl. Phys. A* 707:491 (2002)
89. Hiyama E, et al. *Phys. Rev. C* 66:024007 (2002)
90. Hatsuda T. *Front. Phys. (Beijing)* 13:132105 (2018)
91. Sekihara T, Kamiya Y, Hyodo T. *Phys. Rev. C* 98:015205 (2018)
92. Iritani T, et al. *Phys. Lett. B* 792:284 (2019)
93. Morita K, Ohnishi A, Etminan F, Hatsuda T. *Phys. Rev. C* 94:031901 (2016). Erratum. *Phys. Rev. C* 100:069902 (2019)
94. Etminan F, et al. *Nucl. Phys. A* 928:89 (2014)
95. Hall JMM, et al. *Phys. Rev. Lett.* 114:132002 (2015)
96. Miyahara K, Hyodo T. *Phys. Rev. C* 93:015201 (2016)
97. Kamiya Y, et al. *Phys. Rev. Lett.* 124:132501 (2020)
98. Abd El-Samad S, et al. *Eur. Phys. J. A* 49:41 (2013)
99. Münzer R, et al. *Phys. Lett. B* 785:574 (2018)
100. Borissov A. *EPJ Web Conf.* 222:02002 (2019)
101. Van Buren G. *Rom. Rep. Phys.* 58:069 (2006)
102. Acharya S, et al. *Exploring the NΛ-NΣ coupled system with high precision correlation techniques at the LHC*. Rep. CERN-EP-2021-51, CERN, Geneva (2021)
103. Logoteta D, Vidana I, Bombaci I. *Eur. Phys. J. A* 55:207 (2019)
104. Özel F, Freire P. *Annu. Rev. Astron. Astrophys.* 54:401 (2016)
105. Riley TE, et al. *Astrophys. J. Lett.* 887:L21 (2019)
106. Demorest P, et al. *Nature* 467:1081 (2010)
107. Antoniadis J, et al. *Science* 340:6131 (2013)
108. Cromartie HT, et al. *Nat. Astron.* 4:72 (2019)
109. Djapo H, Schaefer BJ, Wambach J. *Phys. Rev. C* 81:035803 (2010)
110. Tolos L, Fabbietti L. *Prog. Part. Nucl. Phys.* 112:103770 (2020)
111. Weissenborn S, Chatterjee D, Schaffner-Bielich J. *Phys. Rev. C* 85:065802 (2012). Erratum. *Phys. Rev. C* 90:019904 (2014)
112. Haidenbauer J, Meißner UG, Kaiser N, Weise W. *Eur. Phys. J. A* 53:121 (2017)
113. Inoue T. *Proc. Sci.* INPC2016:277 (2016)
114. Schaffner J, Mishustin IN. *Phys. Rev. C* 53:1416 (1996)
115. Hornick N, et al. *Phys. Rev. C* 98:065804 (2018)
116. Acharya S, et al. *Future high-energy pp programme with ALICE*. Rep. ALICE-PUBLIC-2020-005, CERN-LHCC-2020-018, CERN, Geneva (2020)
117. Curceanu C, et al. *Nucl. Phys. A* 914:251 (2013)
118. Gongyo S, et al. *Phys. Rev. Lett.* 120:212001 (2018)
119. Haidenbauer J. *Phys. Rev. C* 102:034001 (2020)
120. Bethe H. *Phys. Rev.* 76:38 (1949)
121. Haidenbauer J, et al. *Nucl. Phys. A* 915:24 (2013)